Mesoscopic fluctuations of the ultrasound attenuation

Selman Hershfield and M. Yu. Reizer
Department of Physics, 174 West 18th Avenue, The Ohio State University, Columbus, Ohio 43210-1106
(Received 5 November 1990; revised manuscript received 25 January 1991)

We compute the fluctuations of the longitudinal sound attenuation rate in mesoscopic metal samples in order to examine the effects of screening in mesoscopic systems. For longitudinal sound attenuation, it is essential to include the screening of the electron-phonon interaction by the electrons. After including both the effects of the fluctuations of the stress tensor and the electron screening, we are able to show that the fluctuations in the longitudinal sound attenuation are of the same order as those of the transverse sound attenuation, where screening is not important. In the limit where the dephasing length is large compared to a side L of the sample cube, the ratio of the fluctuations to the average sound attenuation rate is of order $4\pi(v_F\tau_\varphi)(k_FL)^{-2}$, where τ_φ is the dephasing lifetime and v_F and k_F are the Fermi velocity and wave vector, respectively.

I. INTRODUCTION

A wide variety of mesoscopic fluctuation effects in disordered metal samples has been studied.[1] For most of the effects examined thus far, the fact that the electrons are interacting can be neglected to lowest order in the disorder parameter, $(k_Fl)^{-1}$, where k_F is the Fermi wave vector and l is the electron mean free path. This includes the most extensively studied effect, the conductance fluctuations.[2,3] In this paper we examine the mesoscopic fluctuations of the longitudinal ultrasound attenuation because it is an effect that depends crucially on the electron-electron interaction. Ultrasound attenuation originates from the electron-ion interaction. For longitudinal sound attenuation, the bare electron-ion interaction must be screened by the conduction electrons. Such screening is not important for the transverse sound attenuation. The mesoscopic fluctuations of the transverse sound attenuation have been correctly estimated by Serota.[4] The main contribution of this paper is to show that a similar result to that obtained in Ref. 4 for transverse sound attenuation holds for longitudinal sound attenuation once one takes proper account of the screening.

The paper is organized as follows. In Sec. II we review the moving frame of reference technique for calculating the ultrasound attenuation. In Sec. III we clarify the diagrams necessary for computing the fluctuations of the ultrasound attenuation. Using several identities, we are able to show that large classes of diagrams partially cancel so as to become small. The remaining diagrams are then evaluated to obtain the mesoscopic fluctuations of the ultrasound attenuation. These results are summarized in Sec. IV.

II. ULTRASOUND ATTENUATION IN A BULK METAL

The sound attenuation in disordered metals due to the electron-phonon interaction was first calculated by Pippard[5] using the Boltzmann equation, the Maxwell equations, and charge neutrality. These results were confirmed in microscopic calculations by Schmid[6] and by Grunewald and Sharnberg.[7] In reviewing the microscopic calculation we use the frame of reference moving together with the lattice, which was used by Blount,[8] Tsuneto,[9] and Schmid.[6] This reference frame has the advantage that the impurities are motionless, which allows us to neglect inelastic electron-impurity scattering and hence greatly reduce the number of diagrams that must be considered.

In the moving frame of reference the electron-phonon vertex Γ_0 is equal to

$$\Gamma_0=-i\frac{(\mathbf{p}\cdot\mathbf{q})(\mathbf{p}\cdot\mathbf{e})}{m(2MN\omega_q)^{1/2}}\ , \tag{1}$$

where $\mathbf{p}$ and $\mathbf{q}$ are the electron and phonon momenta and $\mathbf{e}$ is the direction of polarization of the phonon. For longitudinal phonons $\mathbf{e}$ is parallel to $\mathbf{q}$, while for transverse phonons it is perpendicular to $\mathbf{q}$. In Eq. (1) the frequency of the sound is ω_q, m and M are the masses of the electrons and ions, and N is the number density of ions. We will draw these vertices as shown in Fig. 1(a). The basic quantity to be calculated is the phonon self-energy Π. The ultrasound attenuation rate γ is the imaginary part

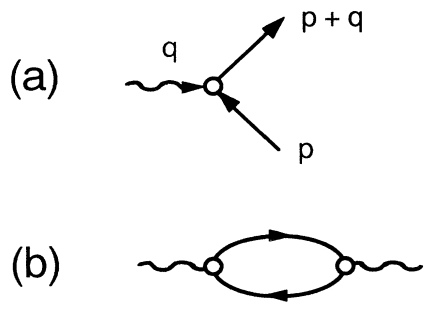

FIG. 1. (a) The bare electron-phonon vertex. (b) A phonon self-energy diagram.

of the self-energy:

$$\gamma = -2\,\mathrm{Im}\{\Pi^r(\mathbf{q},\Omega)\} = i[\Pi^r(\mathbf{q},\Omega) - \Pi^a(\mathbf{q},\Omega)]|_{\Omega=\omega_q} . \tag{2}$$

Because we will be setting Ω equal to ω_q from now on we will use Ω for the phonon frequency.

In Eq. (2), the r and a denote the retarded and advanced part of the phonon self-energy. The simplest diagram for the phonon self-energy is shown in Fig. 1(b). There are two electron-phonon vertices. One is given by Eq. (1), and the other is given by the complex conjugate of Eq. (1). The internal lines are the electron Green's functions. For transverse sound the diagram shown in Fig. 1(b) is sufficient because screening is not important[6,7] and the dressing by impurity lines of the vertex in Eq. (1) is zero. For longitudinal sound attenuation the vertex corrections are not zero, and screening is important.

In order to facilitate the calculation of the longitudinal sound attenuation we will introduce a number of effective vertices and interactions following the conventions of Ref. 10. These will help in the following section, where we calculate the mesoscopic fluctuations of the ultrasound attenuation. In Fig. 2(a) we define the screened Coulomb interaction, $V(q,\omega)$. The relevant vertex correction is defined in Fig. 2(b). From Eq. (2) we see that all we really need to calculate is the retarded self-energy. Thus, for our purposes it will be sufficient to calculate just the retarded part of the screened Coulomb interaction, V^r.

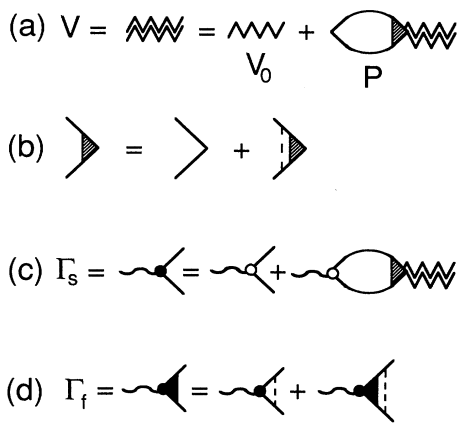

FIG. 2. Effective vertices and interactions. (a) The screened Coulomb interaction in the presence of disorder. (b) Impurity scattering vertex corrections. (c) The screened electron-phonon vertex. (d) The screened electron-phonon vertex with one or more impurity line dressing the vertex.

We begin by calculating the bare electron bubble P_0, which is P of Fig. 2(a) without any vertex corrections. The retarded P_0 is

$$P_0^r(\mathbf{q},\omega) = -i\int\frac{d^3p}{(2\pi)^3}\int\frac{d\varepsilon}{2\pi}\{G^r(\mathbf{p}+q,\varepsilon+\omega)G^a(\mathbf{p},\varepsilon)[S(\varepsilon)-S(\omega+\varepsilon)] + G^a(\mathbf{p}+\mathbf{q},\varepsilon+\omega)G^a(\mathbf{p},\varepsilon)S(\varepsilon+\omega) - G^r(\mathbf{p}+\mathbf{q},\varepsilon+\omega)G^r(\mathbf{p},\varepsilon)S(\varepsilon)\} , \tag{3}$$

where the retarded and advanced Green's functions are G^r and G^a,

$$G^{r(a)}(p,\varepsilon) = [\varepsilon - \varepsilon_p + (-1)i/2\tau]^{-1} , \quad \varepsilon_p = p^2/2m - \mu \tag{4}$$

and $S(\varepsilon)$ is

$$S(\varepsilon) = -\tanh(\varepsilon/2T) . \tag{5}$$

Throughout this paper we use units in which $\hbar$ and k_B are equal to 1. In Eq. (4) the electron-impurity scattering lifetime is τ, and the chemical potential is μ. The first line in Eq. (3) may be evaluated by treating the density of states at the Fermi surface as constant because the principal contribution to the integral comes from electrons near the Fermi surface. If one makes the same approximation for the second and third lines in Eq. (3), one obtains zero because there are either two retarded or two advanced Green's functions in the integral; however, these two terms are not zero when one does the integral exactly because of the factor of $S(\varepsilon)$. The complete result for P_0^r is

$$P_0^r(\mathbf{q},\omega) = -\nu(1+i\omega\tau\zeta_0) , \tag{6}$$

where ν is the density of states at the Fermi surface and ζ_n is the integral,

$$\zeta_n = \frac{1}{\pi\nu\tau}\int\frac{d^3p}{(2\pi)^3}x^n G^r(\mathbf{p}+\mathbf{q},\varepsilon+\omega)G^a(\mathbf{p},\varepsilon), \quad x = \frac{\mathbf{p}\cdot\mathbf{q}}{pq} . \tag{7}$$

The first term in Eq. (6), which is real, comes from the G^rG^r and G^aG^a terms, while the second term comes from the G^rG^a term.

Upon including the vertex corrections depicted in Fig. 2(a), P_0 becomes P, and our result for $P^r(\mathbf{q},\varepsilon)$ is

$$P^r(\mathbf{q},\varepsilon) = -\nu\left[1+\frac{i\omega\tau\zeta_0}{1-\zeta_0}\right] . \tag{8}$$

In the low-frequency, long-wavelength limit, $\omega\tau$, $ql \ll 1$, ζ_0 may be approximated by $1-Dq^2\tau+i\omega\tau$. Here, the electron mean free path and diffusion constant are $l = v_F\tau$ and $D = v_F l/3$, respectively. Substituting into Eq. (8) we find that $P^r(\mathbf{q},\omega)$, which is actually the density-density response function, has the behavior one would expect classically in the diffusive regime:

$$P^r(\mathbf{q},\omega)=-\nu\frac{Dq^2\tau}{Dq^2\tau-i\omega\tau} . \tag{9}$$

It is important to note here that in order to get the correct long-wavelength, low-frequency behavior in Eq. (9), it was necessary to include both the G^aG^a and G^rG^r terms as well as the G^rG^a terms. Had we omitted the G^aG^a and G^rG^r terms, we would have obtained an $i\omega\tau$ in the numerator of Eq. (9) instead of $Dq^2\tau$. This is different from the conductivity, where the G^aG^a and G^rG^r terms are not important when impurity averaging. It is now straightforward to compute the screened electron-electron interaction, $V^r(\mathbf{q},\omega)$, of Fig. 2(a):

$$V^r(\mathbf{q},\omega)=\frac{V_0(q)}{1-P^r(\mathbf{q},\omega)V_0(q)} . \tag{10}$$

The bare electron-electron interaction is $V_0(q)=4\pi e^2/q^2$. Because the phonon wavelengths we are dealing with are much longer than the screening length, Eq. (10) reduces to

$$V^r(\mathbf{q},\omega)=\frac{1}{\nu}\frac{1-\zeta_0}{1-\zeta_0+i\omega\tau\zeta_0} . \tag{11}$$

Before calculating the sound attenuation, it is useful to introduce two effective vertices, Γ_s and Γ_f, shown in Figs. 2(d) and 2(e). For simplicity we do not include the factor g_q,

$$g_q=-i\frac{k_F^2 q}{m(2MN\Omega)^{1/2}} , \tag{12}$$

in the definition of these vertices. These factors will be included in the final result for the sound attenuation rate. The first vertex Γ_s is just the screened longitudinal phonon vertex of Eq. (1):

$$\Gamma_s=x^2-\tfrac{1}{3}+\frac{i\omega\tau(\frac{1}{3}\zeta_0-\zeta_2)}{1-\zeta_0+i\omega\tau\zeta_0} . \tag{13}$$

The vertex Γ_f is the screened vertex with one or more impurity lines dressing the vertex:

$$\Gamma_f=\frac{\zeta_2-\frac{1}{3}\zeta_0}{1-\zeta_0+i\omega\tau\zeta_0} . \tag{14}$$

The screened vertex Γ_s may have any of the three combinations of Green's functions, G^rG^a, G^aG^a, or G^rG^r, attached to it, while the vertex Γ_f may only have G^rG^a attached to it because it is dressed by impurity lines. In the long-wavelength, low-frequency limit these vertices may be approximated by

$$\Gamma_s\approx(x^2-\tfrac{1}{3})+\tfrac{4}{15}i\omega\tau , \tag{15}$$

$$\Gamma_f\approx-\tfrac{4}{15} . \tag{16}$$

A typical diagram contributing to the longitudinal sound attenuation is shown in Fig. 3(a). With the introduction of the effective vertices, we can sum all the diagrams, like the one shown in Fig. 3(a), just by computing the two diagrams shown in Figs. 3(b) and 3(c). In order to avoid overcounting terms, only one of the vertices must be dressed. Evaluating the diagrams of Figs. 3(b) and 3(c) and computing the imaginary part of the self-energy, the Pippard result for the longitudinal sound attenuation rate, γ_l, is obtained:

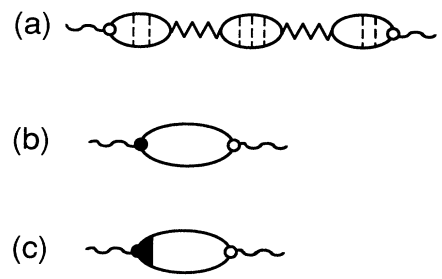

FIG. 3. (a) A typical diagram contributing to the longitudinal phonon self-energy. (b) and (c) The two self-energy diagrams that give the Pippard result for the longitudinal sound attenuation.

$$\gamma_l=\frac{4}{15}\frac{Zm}{M}(qv_F)^2\tau . \tag{17}$$

Here, the average charge per unit cell is Z. For transverse sound one only needs to evaluate the diagram of Fig. 1(b):

$$\gamma_l=\tfrac{3}{4}\gamma_l . \tag{18}$$

Both the longitudinal and transverse sound attenuation rates are proportional to q^2, as expected in the hydrodynamical regime. Equations (17) and (18) depend directly on the phonon momentum rather than their frequency. They may therefore be applied to optical phonons.[10]

III. ULTRASOUND ATTENUATION IN A MESOSCOPIC METAL SAMPLE

A typical diagram that must be considered for the fluctuations of the longitudinal sound attenuation is shown in Fig. 4(a). It consists of two diagrams for the self-energy that have been impurity averaged together. This diagram

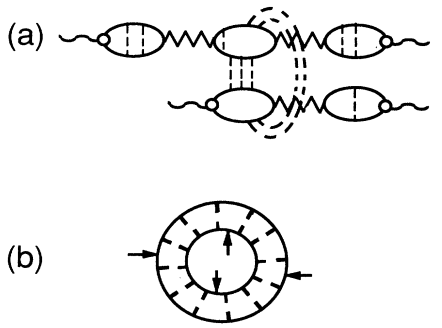

FIG. 4. Diagrams for the mesoscopic fluctuations of the sound attenuation rate. (a) A typical diagram. (b) The structure of a general diagram. The arrows indicate that vertices must be inserted in all possible positions. These vertices may be screened and/or dressed with impurity lines.

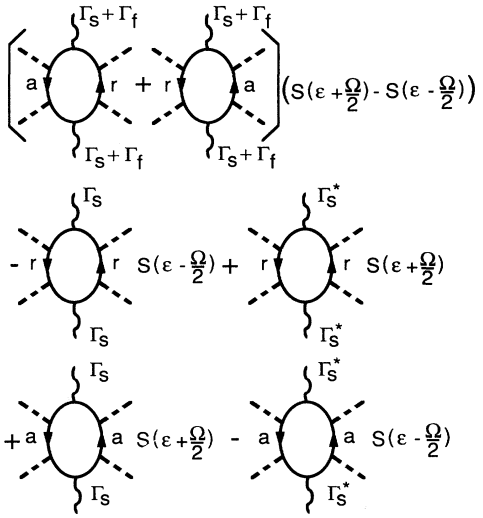

FIG. 5. The different possible inner loops for the diagrams of the form of Fig. 4(b). The vertices Γ_s and Γ_f are defined in the text. The phonon frequency is Ω, and the energies of the Green's functions are $\varepsilon\pm\Omega/2$ as in Eq. (3) with $\omega\rightarrow\Omega$.

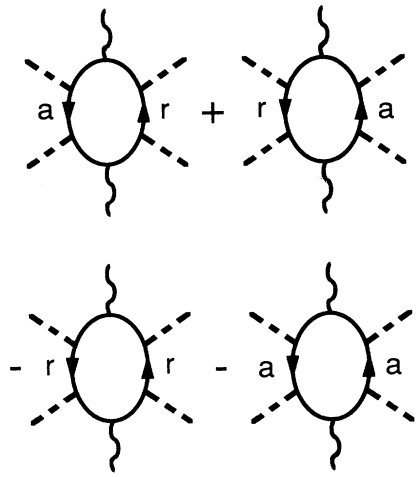

FIG. 6. The four vector-vector vertex inner loops. There is an overall factor of $[S(\varepsilon-\Omega/2)-S(\varepsilon+\Omega/2)]$, which is not shown above.

has only one pair of screening bubbles, which is mutually connected. Diagrams with more than one set of screening bubbles connected are higher order in $(k_F l)^{-1}$. The diagram in Fig. 4(a) also makes it clear that the fluctuations in the longitudinal ultrasound attenuation include fluctuations in the screening. Rather than draw the diagrams as shown in Fig. 4(a), we will be drawing them as shown in Fig. 4(b). The arrows indicate that two vertices must be inserted in all possible positions in each loop. These vertices may contain impurity dressings and screening. In the first part of this section we enumerate the many possible combinations of vertices and retarded and advanced Green's functions. Many of the diagrams will be shown to be small through the use of graphical identities. In the second part of this section the remaining diagrams for the fluctuations in the sound attenuation are evaluated.

To start we focus on only one of the loops in Fig. 4(b). From Eq. (2) the physical quantity that we are calculating is $i(\Pi^r-\Pi^a)$. The different possible inner loops for γ_l are shown in Fig. 5. The energy of the Green's functions is $\varepsilon\pm\Omega/2$, as in Eq. (3), with $\omega\rightarrow\Omega$. The factors of $S(\varepsilon\pm\Omega/2)$ are also the same factors that occur in the imaginary part of Eq. (3). The vertices Γ_s and Γ_f are the ones defined in Eqs. (15) and (16), and the complex conjugate of Γ_s is Γ_s^*. The complex conjugate of $(\Gamma_s+\Gamma_f)$ does not appear in Fig. 5 because we are approximating it to be real:

$$\Gamma_s+\Gamma_f\approx(x^2-\tfrac{1}{3})-\tfrac{4}{15}\ . \tag{19}$$

From Eqs. (15) and (19) all of the vertices in Fig. 5 contain a component whose angular average vanishes $(x^2-\frac{1}{3})$ and a constant term. We will call the $x^2-\frac{1}{3}$ component the vector vertex and the constant term the scalar vertex. Thus, besides the different choices of retarded and advanced Green's functions, there are three possible combination vertices for each loop: two vector vertices, two scalar vertices, or one vector and one scalar vertex. Below we will show that only the terms with two vector vertices are important.

The inner loops with only one vector vertex are shown in Fig. 6. There is a common factor of $[S(\varepsilon-\Omega/2)-S(\varepsilon+\Omega/2)]$, which because the phonon frequency Ω is much less than the temperature may be approximated by $2\Omega(-\partial f/\partial\varepsilon)$ where f is the Fermi function. Thus, the loops with two vector vertices have at least one power of Ω. The factors $|g_q|^2$ give additional powers of q^2 and Ω^{-1}. A power of Ω corresponds to a dimensionless factor of $\Omega\tau$. Likewise, a power of q corresponds to a factor of ql. Thus, all the vector vertex loops are of order $(ql)^2$. Below we will show that the contribution from the vector-scalar loops is at most of order $(ql)^2(\Omega\tau)$, and the contribution from the scalar-scalar loops is at most of order $(ql)^2(\Omega\tau)^2$. In the regime of interest, both ql and $\Omega\tau$ are much less than 1, so it is only necessary to keep all the vector vertex loops. The root-mean-square fluctuations in the sound attenuation rate are proportional to $\tau^{-1}(ql)^2$.

To compute the lowest-order contribution to the ultrasound attenuation, we may set the momentum going into each loop from the vertices equal to zero because higher powers of q correspond to extra factors of ql. This allows us to make use of the following identity, which we write in both momentum space:

$$\frac{1}{\varepsilon-\Omega/2-\varepsilon_p+i/2\tau}\frac{1}{\varepsilon+\Omega/2-\varepsilon_p-i/2\tau}=\frac{1}{i\tau^{-1}+\Omega}\left[\frac{1}{\varepsilon+\Omega/2-\varepsilon_p-i/2\tau}-\frac{1}{\varepsilon-\Omega/2-\varepsilon_p+i/2\tau}\right], \tag{20}$$

and real space:

$$\int d^3x G^a(\mathbf{x},\mathbf{x}',\varepsilon-\Omega/2)G^r(\mathbf{x}',\mathbf{x}'',\varepsilon+\Omega/2)=\frac{1}{i\tau^{-1}+\Omega}[G^a(\mathbf{x},\mathbf{x}'',\varepsilon-\Omega/2)-G^r(\mathbf{x},\mathbf{x}'',\varepsilon+\Omega/2)]\ , \tag{21}$$

$$G^{r(a)}(\mathbf{x},\mathbf{x}',\varepsilon)=\int\frac{d^3p}{(2\pi)^3}e^{i\mathbf{p}\cdot(\mathbf{x}-\mathbf{x}')}G^{r(a)}(\mathbf{p},\varepsilon)\ . \tag{22}$$

Thus, the graph shown at the left-hand side of Fig. 7(a) with a scalar vertex on the top (dot) and either a vector or a scalar vertex on the bottom (arrow) may be written as the difference of the two graphs shown on the right-hand side of Fig. 7(a). The dot in Fig. 7(a) represents a scalar vertex and is not to be confused with the dot in Fig. 2(c), which represents Γ_s. Because Eqs. (20) and (21) are algebraic identities, we can apply this graphical identity independent of what we connect to the inside loop. By adding the graphs with all possible placements of the scalar vertex, there is a cancellation between adjacent placements of the scalar vertex, leaving only $(i\tau^{-1}+\Omega)^{-1}$ times the two graphs shown in Fig. 7(b). If both of the vertices are scalar, there is an additional cancellation that takes place upon adding the two diagrams like the one shown in Fig. 7(c). This cancellation reduces the prefactor of the two diagrams in Fig. 7(b) from $(i\tau^{-1}+\Omega)^{-1}$ to $\Omega(i\tau^{-1}+\Omega)^{-2}$. Identities similar to the ones in Eqs. (20) and (21) may also be applied to scalar vertices with two advanced Green's functions or two retarded Green's functions:

$$G^{r(a)}(\mathbf{p},\varepsilon-\Omega/2)G^{r(a)}(\mathbf{p},\varepsilon+\Omega/2)$$
$$=\frac{1}{\Omega}[G^{r(a)}(\mathbf{p},\varepsilon+\Omega/2)-G^{r(a)}(\mathbf{p},\varepsilon-\Omega/2)]\ . \tag{23}$$

The only difference between the G^aG^a or G^rG^r cases and the G^aG^r case is that diagrams like the one in Fig. 7(c) are zero. The identities of Eqs. (20)–(23) have been applied previously in conductance fluctuation calculations to show that a certain class of very large diagrams is actually zero.[11] They can also be used to show that the density-density response function and the mesoscopic fluctuations of the density-density response function are zero in the limit as $q\to 0$. This is just the statement that the total number of particles is fixed.

At this point we are prepared to show that the scalar-scalar and scalar-vector loops are smaller than the vector-vector loops by factors of $\Omega\tau$. If one applies the above identities to the scalar-scalar parts of the diagrams in Fig. 5, one finds that to lowest order in $\Omega\tau$ the sum of the diagrams with all possible placements of one scalar vertex, including diagrams like the one in Fig. 7(c), is just the difference of the two diagrams in Fig. 7(b) multiplied by

$$(\tfrac{4}{15})^2 2i\Omega^2\tau^3[S(\varepsilon-\Omega/2)-S(\varepsilon+\Omega/2)]\ . \tag{24}$$

As for the vector-vector loops, the difference of the S

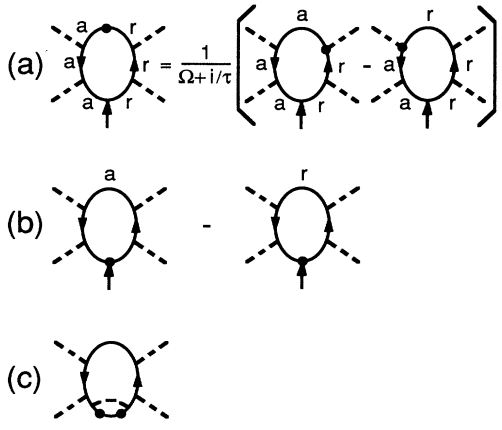

FIG. 7. Graphical identities. (a) The basic identity. The dot on the top denotes a scalar vertex and is not to be confused with Γ_s of Fig. 2(c). (b) The two diagrams that remain after summing over all possible placements of the scalar vertex in (a). (c) Additional inner loops that are important if both of the vertices are scalar vertices.

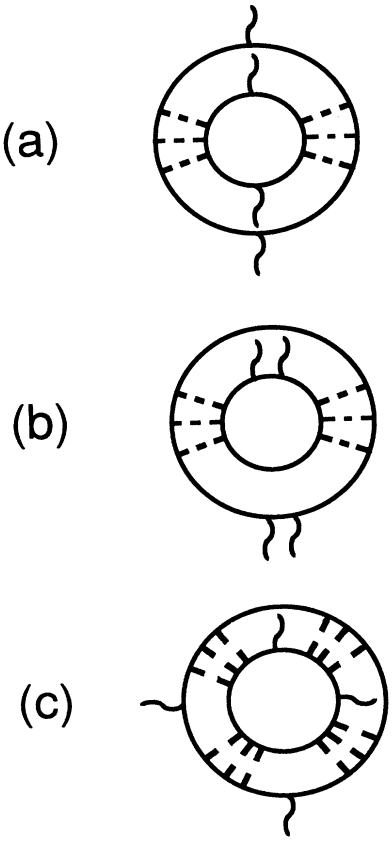

FIG. 8. Diagrams for the fluctuations of the sound attenuation rate. (a) and (b) The most-singular diagrams. (c) A less-singular diagram.

functions gives one power of Ω. Thus, Eq. (24) has three powers of Ω. Including the power of Ω^{-1} from $|g_q|^2$, there is a net power of Ω^2 from the scalar-scalar loops, which makes them much smaller than the vector-vector loops by $(\Omega\tau)^2$. If one applies the above identities to the vector-scalar parts of the diagrams in Fig. 5, one finds that to lowest order in $\Omega\tau$ the vector-scalar loops give a contribution that is $i(\frac{16}{15})\Omega\tau$ times the derivative $\partial/\partial\varepsilon$ of the product of $S(\varepsilon)$ and the two diagrams in Fig. 7(b). The integral of a total derivative is zero provided that the function one is differentiating decays at $\pm\infty$. The function $S(\varepsilon)$ does not decay as $\varepsilon\rightarrow\pm\infty$; however, the diagrams of Fig. 7(b) when connected to the outside loop involve impurity ladders, which decay for energies far from the Fermi surface. Thus, the vector-scalar loops must have at least a power of Ω^2, which when multiplied by the Ω^{-1} from $|g_q|^2$ gives a net factor of $\Omega\tau$. The vector-scalar loops are also smaller than the vector-vector loops. This completes our proof that only the vector-vector loops are important to lowest order in $\Omega\tau$.

At this point we must evaluate the diagrams like the one shown in Fig. 4(b) with all vector vertices and any of the combinations of retarded and advanced Green's functions shown in Fig. 6. These diagrams are similar to the ones for the conductance fluctuations, except that the vertices are not current vertices, but the stress vertex $x^2-\frac{1}{3}$ and loops containing all advanced or all retarded Green's functions do contribute. For the conductance there are no loops with all retarded or advanced Green's functions.[12,13] Three possible diagrams are shown in Fig. 8. If the diffusion propagators (ladder sums) carry momentum k, then these diagrams have poles proportional to k^{-4}. The diagram in Fig. 8(c) has four diffusion propagators, giving a factor of k^{-8}; however, each of the $x^2-\frac{1}{3}$ vector vertices occurring by itself gives a factor of k^2 so that the diagram in Fig. 8(c) actually has no singularity, i.e., it is proportional to k^0. In a similar manner one can show that the most divergent diagrams are the ones in Figs. 8(a) and 8(b). Summing all such diagrams, the mean square fluctuations of the ultrasound attenuation are

$$\frac{\langle(\delta\gamma_l)^2\rangle}{\langle\gamma_l\rangle^2}=\frac{8}{9}\frac{(k_F l)^2}{(n_{el}L^3)^2}\int\frac{d\varepsilon}{2\pi}\left[\frac{-\partial f}{\partial\varepsilon}\right]\int\frac{d\varepsilon'}{2\pi}\left[\frac{-\partial f}{\partial\varepsilon'}\right]\sum_m\left[4|\lambda_m|^{-2}+12\,\mathrm{Re}(\lambda_m^{-2})\right], \tag{25}$$

$$\lambda_m=D\tau\left[\frac{\pi}{L}\right]^2(m_x^2+m_y^2+m_z^2)-i(\varepsilon-\varepsilon')\tau+\tau/\tau_\varphi\ . \tag{26}$$

Here we have assumed that the sample is a cube of side L. The dephasing lifetime is τ_φ, and n_{el} is the density of electrons. Because we have an isolated sample, the integers m_i take on the values $0,1,2,\ldots$.[4] The angular brackets in Eq. (25) denote the average over the impurity configuration at zero magnetic field. As usual if one measures the fluctuations for a given sample as a function of magnetic field, the result is reduced by a factor of 2.[2] For transverse sound attenuation, where screening is not important, one sums the same set of diagrams, except that the bare transverse phonon vertex of Eq. (1) replaces $x^2-\frac{1}{3}$. This just changes the result of Eq. (25) by a constant factor in such a way that

$$\frac{\langle(\delta\gamma_t)^2\rangle}{\langle\gamma_t\rangle^2}=\frac{\langle(\delta\gamma_l)^2\rangle}{\langle\gamma_l\rangle^2}\ . \tag{27}$$

An estimate in the fractional change in the sound attenuation in the limit where the dephasing length is long compared to the sample length is obtained by only keeping the $m_i=0$ term in the sum of Eq. (25):

$$\frac{\delta\gamma_l}{\gamma_l},\ \frac{\delta\gamma_t}{\gamma_t}=4\pi\left[\frac{v_F\tau_\varphi}{L}\right]\frac{1}{(k_FL)^2}\ . \tag{28}$$

Although $v_F\tau_\varphi$ may be larger than L and 4π gives an order of magnitude, the factor of $(k_FL)^2$ is much greater than 1 for a typical metal sample. Thus, the fluctuations in the ultrasound attenuation are very small.

IV. SUMMARY

In conclusion, we have computed the mesoscopic fluctuations of the ultrasound attenuation in impure metals. After carefully taking into account the effects of the screening by the electrons, the fluctuations of the longitudinal sound attenuation were shown to be of the same size as the transverse sound attenuation. Physically this means that for characteristic values of the sound frequency and wave number the condition of electroneutrality is valid, and the mesoscopic fluctuations of the electron-electron and electron-ion interactions are small. The size of both the longitudinal and transverse sound attenuation fluctuations is very small compared to their average value.

ACKNOWLEDGMENTS

This work was supported in part by the U.S. Office of Naval Research (S.H.) and in part by the Department of Energy–Basic Energy Sciences, Division of Materials Research (M.R.).

[1]B. Al'tshuler, P. Lee, and R. Webb, Quantum Effects in Small Disordered Systems (Elsevier, Amsterdam, in press).
[2]P. A. Lee, A. D. Stone, and H. Fukuyama, Phys. Rev. B **35**, 1039 (1987).
[3]S. Washburn and R. A. Webb, Adv. Phys. **35**, 375 (1986).
[4]R. A. Serota, Phys. Rev. B **38**, 12 640 (1988).
[5]A. B. Pippard, Philos. Mag. **46**, 1104 (1955).
[6]A. Schmid, Z. Phys. **259**, 421 (1973).
[7]G. Grunevald and K. Sharnberg, Z. Phys. **268**, 197 (1974); Z. Phys. B **20**, 61 (1975).
[8]E. L. Blount, Phys. Rev. **114**, 418 (1959).
[9]T. Tsuneto, Phys. Rev. **121**, 402 (1961).
[10]M. Yu. Reizer, Phys. Rev. B **40**, 7461 (1989).
[11]S. Hershfield, Ann. Phys. (N.Y.) **196**, 12 (1989).
[12]B. L. Al'tshuler and B. I. Shkovskii, Zh. Eksp. Teor. Fiz. **91**, 220 (1986) [Sov. Phys.—JETP **64**, 127 (1986)].
[13]C. L. Kane, R. A. Serota, and P. A. Lee, Phys. Rev. B **37**, 6701 (1988).